

THE EQUATION OF STATE OF MH-III: A POSSIBLE DEEP CH₄ RESERVOIR IN TITAN, SUPER-TITAN EXOPLANETS AND MOONS

A. LEVI

Harvard-Smithsonian Center for Astrophysics, 60 Garden Street, Cambridge, MA 02138, USA

R. E. COHEN

Extreme Materials Initiative, Geophysical Laboratory, Carnegie Institution for Science 5251 Broad Branch Rd. NW, Washington, DC 20015, USA

and

Department of Earth and Environmental Sciences, Ludwig-Maximilians University Munich, Theresienstrasse 41, Munich 80333, Germany

ABSTRACT

We investigate the thermal equation of state, bulk modulus, thermal expansion coefficient, and heat capacity of MH-III (CH₄ filled-ice Ih), needed for the study of CH₄ transport and outgassing for the case of Titan and super-Titans. We employ density functional theory and *ab initio* molecular dynamics simulations in the generalized-gradient approximation with a van der Waals functional. We examine the finite temperature range of 300 K-500 K and pressures between 2 GPa-7 GPa. We find that in this P-T range MH-III is less dense than liquid water.

There is uncertainty in the normalized moment of inertia (MOI) of Titan; it is estimated to be in the range of 0.33 – 0.34. If Titan’s MOI is 0.34, MH-III is not stable at present in Titan’s interior, yielding an easier path for the outgassing of CH₄. However, for an MOI of 0.33, MH-III is thermodynamically stable at the bottom of a ice-rock internal layer capable of storing CH₄. For rock mass fractions $\lesssim 0.2$ upwelling melt is likely hot enough to dissociate MH-III along its path. For super-Titans considering a mixture of MH-III and ice VII, melt is always positively buoyant if the H₂O:CH₄ mole fraction is > 5.5 . Our thermal evolution model shows that MH-III may be present today in Titan’s core, confined to a thin (≈ 10 km) outer shell. We find that the heat capacity of MH-III is higher than measured values for pure water-ice, larger than heat capacity often adopted for ice-rock mixtures with implications for internal heating.

1. INTRODUCTION

Extraterrestrial habitability has always fascinated humanity. The discovery of exoplanets makes the question of habitability of much practical importance. Current and future space missions, such as the Transiting Exoplanet Survey Satellite (TESS) and James Webb Space Telescope (JWST), will provide us with spectroscopic atmospheric characterizations. Improving constraints on habitability will provide us with better target filters for future observations.

Metabolism requires energy, which life obtains in the process of electron transfer by redox chemical reactions (McKay 2014; Jelen et al. 2016). One such reaction, analogous to photosynthesis on Earth, and invoked as a possible source of energy for life on Titan, is the production of organics from CH₄, followed by release of H₂. In addition, for the cryogenic temperatures on the surface of Titan, CH₄ replaces water as the surface liquid body, which is essential for cycling nutrients (McKay 2016). Titan-like worlds may be favorable for habitability being out of harms reach around highly active M-dwarfs (Lunine 2009), and should be common throughout our cosmos considering the ubiquity of water. Generalizing beyond Titan-like worlds, CH₄, in conjunction with atmospheric O₂ and O₃, is speculated to be a biosignature (Kaltenegger et al. 2010). Therefore, modeling the transport of CH₄ across the interiors of planets and moons, and its availability at the surface and atmosphere, are of paramount importance.

Clearly, the data we have for Titan is far superior to what we will have in the foreseeable future for Titan-like exoplanets and exomoons. Therefore, although our aim is more general, this work will use Titan as our primary

model object. During the epoch of its accretion Titan maintained an inner core of undifferentiated ice-rock mixture (Lunine & Stevenson 1987; Barr et al. 2010; Monteux et al. 2014). The ultimate source of CH_4 in present day Titan’s atmosphere is this inner core (Lunine & Stevenson 1987). However, this implies that CH_4 was able to traverse across the entire depth of Titan to reach the atmosphere.

The moment of inertia estimated for Titan from Cassini gravity measurements suggests that Titan’s interior is partially undifferentiated. The nature of the undifferentiated layer is still unknown. It may be either an ice-rock layer between a rocky core and a water rich outer mantle, or an outer rocky core composed of hydrous silicates (Fortes 2012; Lunine et al. 2010). If a mixed ice-rock layer indeed exists in the interior of Titan, then a newly discovered high pressure solid solution in the H_2O - CH_4 binary system called MH-III (also CH_4 filled-ice Ih) may hinder the outer transport of internal CH_4 into the atmosphere.

The formation of MH-III was first reported in Loveday et al. (2001a). Contrary to what was previously assumed for the H_2O - CH_4 system, upon increasing the pressure above about 2 GPa, at room temperature, the classical structure H cage clathrate transforms into MH-III, rather than experience phase separation into water ice VII and solid CH_4 . In this way the solubility of H_2O and CH_4 is kept throughout the entire pressure range inside Titan. This is also likely true for the much higher pressures spanning water ice mantles of water-rich exoplanets, given that MH-III was found to be stable up to about 100 GPa (Hirai et al. 2006), and temperatures higher than 1000 K (ichi Machida et al. 2006). We refer the reader to Loveday et al. (2001b) for a detailed description of the crystallographic nature of MH-III.

If CH_4 is indeed locked in grains of MH-III, scattered within a deep ice-rock layer above the rocky core of Titan, then how much of it may be transported outward depends on the buoyancy of these grains with respect to melt pockets and the solubility of CH_4 under such conditions. Such an analysis requires thermophysical data for MH-III at the appropriate conditions. In the context of Titan-like exoplanets, previous work on the transport of CH_4 across the interior pinpointed the necessary thermophysical data and the lack thereof (Levi et al. 2013; Levi et al. 2014). Quantifying the needed thermophysical data is the prime object of this work.

In section 2 we probe the pressure regime in a possible undifferentiated ice-rock layer inside Titan, to better pinpoint our molecular simulations and the possible role of MH-III. In section 3 we explain our computational methods. In section 4 we derive the thermal equation of state and thermal expansivity. Section 5 is dedicated to the heat capacity. In section 6 we estimate the thickness of a MH-III enriched layer in Titan’s interior, and its carbon content capacity. In section 7 we use a 1-D thermal evolution model to assess the stability of such a layer. Section 8 is a discussion, and section 9 is a summary.

2. THE PRESSURE REGIME IN THE UNDIFFERENTIATED ICE-ROCK LAYER

In this section we estimate the pressure at the boundary between a possible internal ice-rock layer and Titan’s inner rocky core. We consider three basic constraints for Titan, its radius, mass and normalized moment of inertia (MOI). We adopt a layered model for the internal structure (see Fig.1). The outermost condensed layer is a shell composed of ice Ih with a mass density of 0.917 g cm^{-3} . We assume for this outer shell a mean thickness of 100 km (Nimmo & Bills 2010). Underlying the outermost shell is likely a subterranean ocean. Baland et al. (2014) argue for an ocean thickness of less than 100 km, whereas Lunine et al. (2010) list models where the ocean is thicker than 200 km. Here, we adopt a width of 200 km for the ocean.

The density range for the subterranean ocean may be inferred from the observational data. It is likely denser than pure water (Iess et al. 2012). Baland et al. (2014) suggest an ocean rich in salts with a mass density in the range $1.275 - 1.350 \text{ g cm}^{-3}$. Mitri et al. (2014) argue that an ocean denser than 1.2 g cm^{-3} is inferred from the observed tidal Love number. While the latter is gravitationally compatible with a seafloor composed of ice V, the former range calls for ice VI or VII. Baland et al. (2014) suggest that rock or salt impurities in ice III (1.16 g cm^{-3}) can increase the overall density and stabilize an overlying dense ocean. This likely requires strict criteria of size and distribution of rock in the ice, and needs proof. Salty-ice, high-pressure ice with interstitial ions, is another possibility for a density-increasing impurity. However, contrary to ice VII, ions of salt are not very compatible within the smaller voids of ice VI (Frank et al. 2006; Journaux et al. 2017), and no information is available for the case of ice V. Here we avoid this complication by restricting the ocean density to that of ice V, the high-pressure phase composing the ocean floor, as deduced from our model.

Beneath the ocean is a high pressure water ice layer, which according to the pressure derived can be composed of either water ice V or VI. We consider the thickness of this layer to be a free parameter, and is here constrained by the observational data.

An undifferentiated ice-rock layer is a possible buffer between the high-pressure water ice layer and a rocky core (Iess et al. 2010). Its width is taken to be a free parameter, to be estimated by the observational data. If the mass

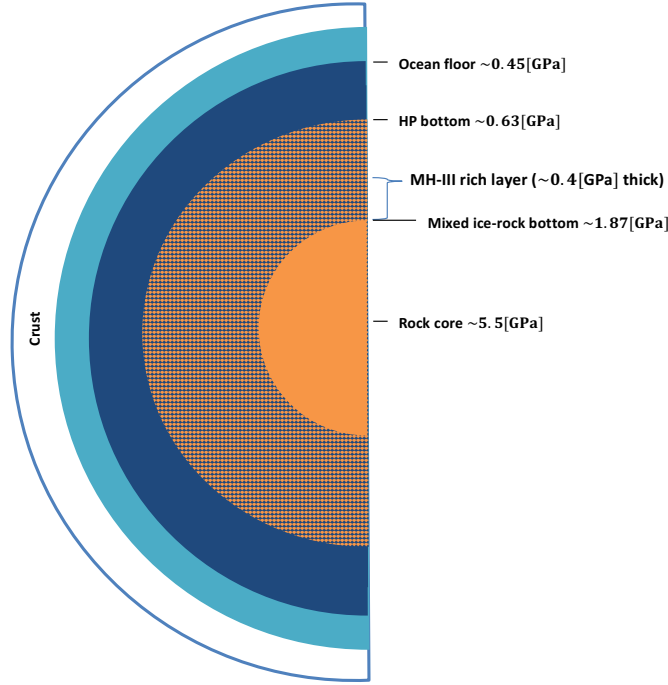


Figure 1. A layered model for Titan: crust, subterranean ocean, high-pressure water ice layer, mixed ice-rock layer, and a rocky core. A layer enriched in MH-III may reside above the core.

fraction of rock composing this layer is χ , the mixed layer mass density is:

$$\rho_{mix} = \frac{\rho_{hp}\rho_{rock}}{(1 - \chi)\rho_{rock} + \chi\rho_{hp}} \quad (1)$$

where ρ_{rock} and ρ_{hp} are the rock and high-pressure water ice polymorph densities, respectively. Below we assume $\chi = 0.5$.

The mass density of a rock depends on its composition. Values may range from as little as 2.5 g cm^{-3} for hydrated rock to as high as 4.5 g cm^{-3} for anhydrous rock mixed with iron (see discussion in [Sohl et al. 2003](#)). [Castillo-Rogez & Lunine \(2010\)](#) suggest that carbonaceous and ordinary chondrites are good references for hydrous and anhydrous rock, respectively. A study of carbonaceous chondrites shows they have a wide range of possible grain densities, ranging from 2.42 g cm^{-3} to 5.66 g cm^{-3} , with an average sample value of 3.44 g cm^{-3} ([Macke et al. 2011](#)). For some specimens bulk density and grain density vary widely due to high porosity. For ordinary chondrites, the average grain density varies from 3.55 g cm^{-3} to 3.77 g cm^{-3} , for LL and H type, respectively ([Consolmagno et al. 2006](#)). High-temperature and pressure in the interior of Titan likely reduce porosity. In any case grain densities should be considered as upper boundary values. [Baland et al. \(2014\)](#) infer a very high density for Titan's core (between 3.39 and 4.50 g cm^{-3}), implying a high fraction of iron. Therefore, we solve our model for these higher rock mass densities as well, even though they deviate from averaged values.

Finally, the MOI for Titan probably falls in the range of $0.33 - 0.34$. Non-hydrostatic corrections would favor the lower value. For an in depth discussion over the MOI we refer the reader to [Lunine et al. \(2010\)](#), [Iess et al. \(2010\)](#), [Baland et al. \(2014\)](#), and [Mitri et al. \(2014\)](#).

We solve for the internal structure of Titan by considering a grid of possible values for the thickness of the high-pressure water ice layer, and the undifferentiated ice-rock layer. This produces contour maps of iso-mass and iso-MOI lines. The solution for the internal structure is obtained by superimposing such two maps, pinpointing the crossing point of the proper contours.

In [Fig.2](#) and [Fig.3](#) we give our solutions for a MOI of 0.33 and 0.34 , respectively. For a given mass, radius and MOI, increasing the rock mass density requires decreasing the core size and increasing the extent of the mixed ice-rock layer. This results in a monotonic increase in pressure at the bottom of the undifferentiated ice-rock layer.

The higher MOI commands a body less differentiated. In our model increasing the rock mass density, given a rocky core, is in favor of a lower MOI. This is compensated by thickening of the undifferentiated mixed ice-rock layer and

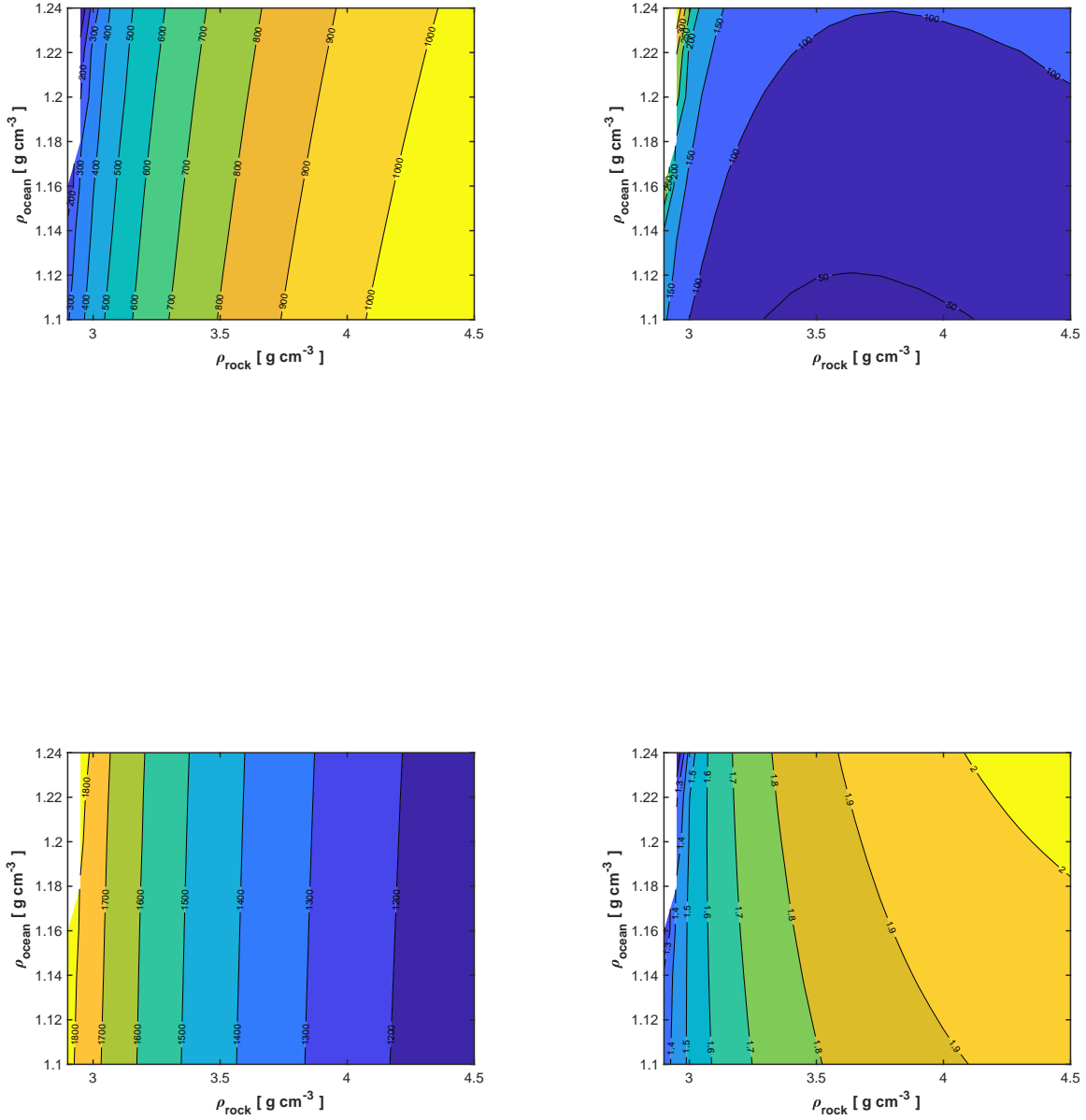


Figure 2. Thickness [km] of the undifferentiated ice-rock layer (**upper left panel**), thickness [km] of the high-pressure ice layer underlying a subterranean ocean (**upper right panel**), radius [km] of the rocky core (**bottom left panel**), and pressure [GPa] at the boundary between the rocky core and a possible undifferentiated ice-rock layer (**bottom right panel**), as a function of rock and ocean mass densities. Data is for a normalized moment of inertia of 0.33. We assume that the mass fraction of rock in the undifferentiated ice-rock layer is 0.5. White space is where no solution is found for the given model.

thinning of the high pressure water-rich ice layer which has a lower density. This compensation is more severe the larger is the MOI, therefore resulting in a more constrained solution.

The possible subterranean ocean represents an outer layer. Therefore, a low mass density for its aqueous solution would favor a low MOI. Hence, the sweeter the subterranean ocean is, the tighter is the constraint on the rock composition (see Fig.3).

The result of this interplay in the internal structure yields a distinction between the two moments of inertia. In order to determine whether this distinction is also manifested in the ability to outgas CH_4 , and the role of MH-III, we need the thermophysical parameters of MH-III. This is the subject of the following sections.

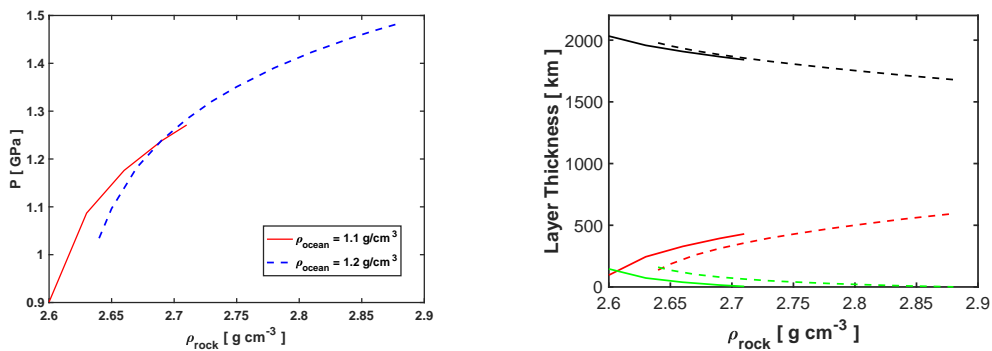


Figure 3. (left panel) Pressure at the boundary between the rocky core and a possible undifferentiated ice-rock layer versus rock mass density. **(right panel)** Titan's interior structure versus rock mass density, where black curves represent the radius of the core (d_c), red curves represent the thickness of the undifferentiated mixed ice-rock layer (d_{mix}), and green curves represent the thickness of the high-pressure ice layer (d_{hp}). In both panels the solid curves are for an ocean mass density of 1.1 g cm^{-3} , and dashed curves are for an ocean mass density of 1.2 g cm^{-3} . The normalized moment of inertia (MOI) here is 0.34.

3. COMPUTATIONAL METHODS

We studied the equation of state of MH-III using first-principles electronic structure methods. We performed both static total energy relaxations and molecular dynamics (MD) simulations with the CP2K code. Simulations were carried out using the CSVR thermostat, which was shown to produce for ice I_h the same vibrational spectrum as that derived with the microcanonical ensemble (Bussi et al. 2007).

Throughout this work we use the quickstep framework within CP2K, with the Gaussian and plane waves mixed bases (GPW). We use the Gaussian basis sets (DZVP-MOLOPT-GTH) from VandeVondele et al. (2005), VandeVondele & Hutter (2007), in conjunction with the pseudopotentials (GTH-PBE) of Goedecker, Teter, and Hutter (Goedecker et al. 1996; Hartwigsen et al. 1998; Krack 2005). Our system is converged with a cutoff energy of 480 Ry.

We use the exchange functional XC_GGA_X_RPW86 from Marques et al. (2012), and an LDA local correlation functional of Vosko et al. (1980), with the non-local van der Waals correlation functional of Lee et al. (2010), adopting a cutoff energy of 160 Ry for the latter.

We use VESTA to produce various super cells ($2 \times 1 \times 1$, $2 \times 2 \times 1$ and $2 \times 2 \times 2$) from an experimental structure, and AVOGADRO to add the hydrogens since the experiments could not constrain the H positions. We test this procedure by calculating the static energy per supercell, yielding the average energy per atom, with an absolute average deviation of 0.004%. We also derived the static unit cell energy for various \mathbf{k} -grids (Γ , Monkhorst-Pack (MK): 2 2 2, 4 4 4, 6 4 4, 8 4 4, 8 8 8). The difference between Γ and MK 8 8 8 was found to be $0.0002 \text{ Ha atom}^{-1}$. We also tested for proper

energy scaling between the primitive cell and our largest supercell. First, we optimized the unit cell at 0 K adopting Macdonald $2 \times 2 \times 2$ for the \mathbf{k} -grid, and derived its associated energy. Then, the optimized crystal was used to build the supercell, whose energy was calculated adopting Γ sampling only. Both derived energies are in agreement to 0.0023%.

We derived the 0 K equation of state (EOS) by optimizing the crystal structure of the unit cell using three different \mathbf{k} -point sets: Γ , Macdonald $2 \times 2 \times 2$ and MK $8 \times 4 \times 4$. This was used as a double test prior to MD simulations: (1) to check for a normal P-V relation, and (2) check that the optimized cell parameters are in agreement with experimental data given at room temperature.

Our finite temperature MD was performed on a $(2 \times 2 \times 2)$ supercell composed of 352 atoms (each unit cell consists of eight H_2O molecules and four CH_4 molecules). All simulations carried out on the supercell using Γ sampling only. Prior to the MD runs the supercell was optimized at 0 K and the resulting cell parameters were used for our finite temperature NVT simulations. In table 1 we summarize our derived cell parameters, at 0 K, for our imposed external pressures.

Table 1. Unit cell parameters and volume of MH-III from optimization of the supercell at 0 K.

P [GPa]	a [Å]	b [Å]	c [Å]	V [Å ³]
2	4.786	8.272	8.004	316.818
3	4.761	8.279	7.673	302.369
4	4.674	8.186	7.591	290.374
5	4.676	8.141	7.414	282.212

Each MD simulation started with a thermalization run until the pressure changed by less than a few percent. Production runs had 20000 steps per run, with a time step of 0.5 fs. Such a runtime was found adequate for producing frequency spectra from the velocity autocorrelation for pure water systems (French & Redmer 2015). We further tested for the effect of the time step by performing shorter runs (10000 steps) adopting a time step of 0.3 fs. The latter runs agree well with the former runs using the larger time step.

Convergence was tested using block sampling. Pressure fluctuations are found to agree with theoretical constraints (see page 341 in Landau & Lifshitz 2007). Thermal averages reported in this work used only the last two thirds of each MD run.

4. THERMAL EQUATION OF STATE

For the equation of state (EOS) we use the following form,

$$V(P, T) = V(P, 0 \text{ K}) \exp \left[\int_{0 \text{ K}}^T \alpha(P, T) dT \right] \quad (2)$$

where V is the volume per atom, P is pressure, T is the absolute temperature, and α is the volume coefficient of thermal expansion.

For the 0 K EOS we use a form of the Murnaghan equation,

$$V(P, 0 \text{ K}) = V_0 \left(\frac{B_0 + \tilde{B}_0 P}{B_0 + \tilde{B}_0 P_0} \right)^{-1/\tilde{B}_0} \quad (3)$$

where B_0 and \tilde{B}_0 are the isothermal bulk modulus and its pressure derivative, respectively, at 0 K.

For the volume coefficient of thermal expansion we assume a similar form to that in Fei et al. (1993),

$$\alpha(P, T) = \alpha_0(T) \left(\frac{B_0 + \tilde{B}_0 P}{B_0 + \tilde{B}_0 P_0} \right)^{-\eta} \quad (4)$$

In Fig.4 we give our results together with published experimental data. A comparison with the experimental data shows that our simulations systematically overestimate the pressure by 1 GPa. A systematic deviation is likely caused by inaccuracies in the representation of the exchange and correlation functionals, resulting in a systematic error in bond strengths (Lejaeghere et al. 2014). For hydrogen-bonded crystals a systematic shift of approximately 1 GPa has previously been reported (e.g. Brand et al. 2010). A systematic error in DFT calculations can be corrected to improve predictability of experimental results (Lejaeghere et al. 2014). Indeed, by subtracting 1 GPa our results match the experimental data (at 300 K and 400 K) well. This is used here to benchmark the magnitude of the systematic deviation. The parameters of the EOS are obtained by a fit to the experimental data and to the data derived in this work after shifting it by 1 GPa. Our EOS with the parameters given below fit the data sets with an absolute average deviation of 0.31%.

For $P_0 = 0$ GPa we find the following values with 1σ error bars: $V_0 = 7.341 \pm 0.010 \text{ \AA}^3/\text{atom}$, $B_0 = 19.72 \pm 0.55$ GPa and $\tilde{B}_0 = 4.133 \pm 0.188$.

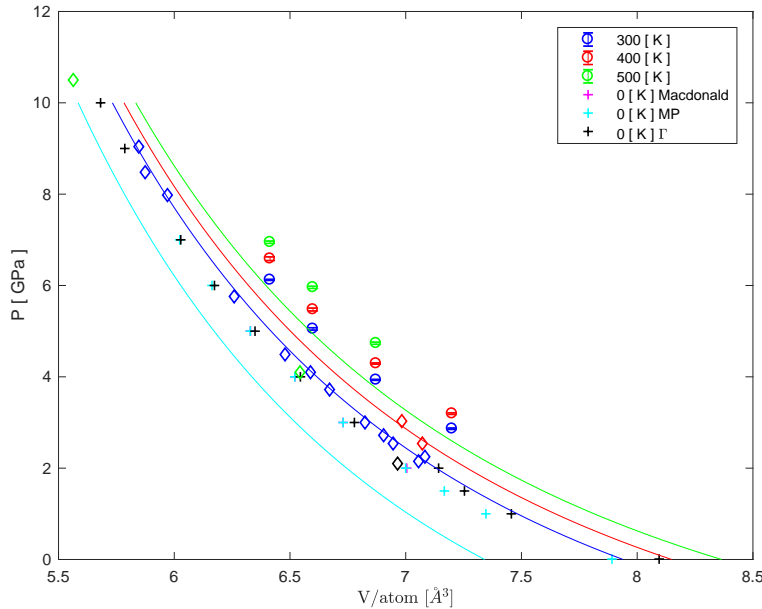


Figure 4. Pressure versus volume per atom for the four isotherms studied in this work. Experimental data: (blue diamonds) room temperature data from Loveday et al. (2001a), (green diamonds) room temperature data from Hirai et al. (2003), (red diamonds) is data from Bezacier et al. (2014b) at about 400 K, (black diamond) is data from Baumert et al. (2005). Our simulations at: 500 K, 400 K and 300 K are the: green, red and blue circles respectively. Black, cyan and magenta crosses are the 0 K results of this work using \mathbf{k} -grids of: gamma, Monkhorst-Pack $8 \times 4 \times 4$ and Macdonald respectively.

In table 2 we compare between the unit cell parameters at 300 K from experiment and our derived values before and after the 1 GPa shift in pressure. First the EOS is used in order to determine the unit cell volume at the pressure and temperature of the reference experiment, and then the relation between the cell parameters and the volume, that we have obtained by cell optimization, is used to infer the former. The relation between the cell parameters and the volume is given in Fig.5.

Table 2. Unit cell parameters of MH-III at 300 K. The experimental data (subindex *exp*) at room temperature, is taken from [Loveday et al. \(2001a\)](#) for 3 GPa and from [Hirai et al. \(2003\)](#) for 4 GPa. Original simulation results have subindex *cal*, and shifted data is subindex *sh*.

P [GPa]	a_{exp} [Å]	b_{exp} [Å]	c_{exp} [Å]	a_{cal} [Å]	b_{cal} [Å]	c_{cal} [Å]	a_{sh} [Å]	b_{sh} [Å]	c_{sh} [Å]
3	4.746	8.064	7.845	4.809	8.219	7.923	4.746	8.141	7.787
4	4.687	7.974	7.704	4.746	8.141	7.787	4.692	8.070	7.678

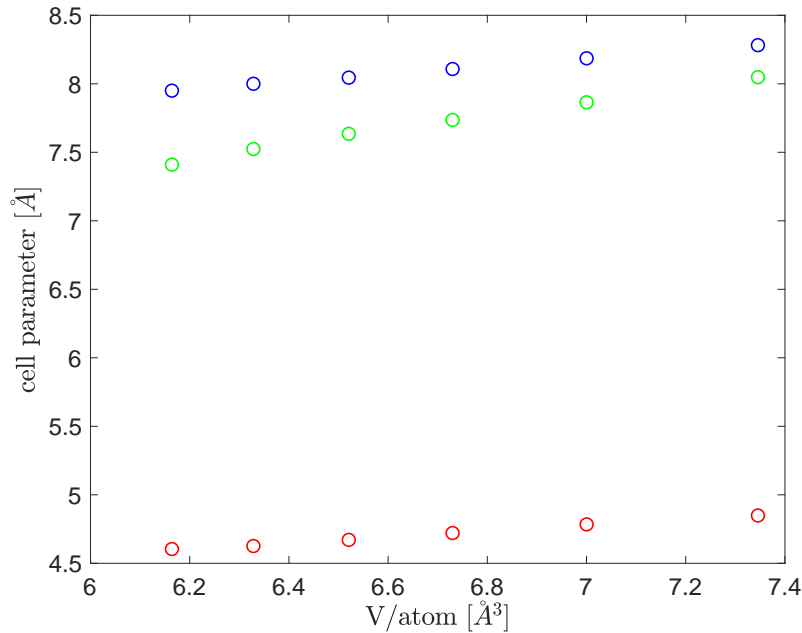


Figure 5. Unit cell parameters of MH-III versus volume per atom, a, b and c are red, blue and green, respectively.

For the volume thermal expansion coefficient we find that a constant value for α_0 of $2.458 \times 10^{-4} \pm (1.68 \times 10^{-5}) \text{ K}^{-1}$, and $\eta = 0.923 \pm 0.121$, best fit the data. An investigation of ice VII in the pressure range of 0–10 GPa and temperature range of 300–450 K detected no temperature dependence for α_0 ([Bezacier et al. 2014a](#)). However, an earlier work suggested a linear dependence on the temperature ([Fei et al. 1993](#)). We note that our modeling approach was shown to produce ice VII lattice parameters that are in good agreement with experimental data (e.g. [Futera & English 2018](#)). In Fig. 6 we show our derived thermal expansion coefficient for MH-III and that for ice VII, to aid in comparison between the two phases. For this purpose we fit our suggested equation of state to the data in [Bezacier et al. \(2014a\)](#) with an absolute average deviation of 0.25%. We adopt the bulk modulus and thermal expansion coefficient of [Bezacier et al. \(2014a\)](#).

At room temperature the thermal expansion coefficient for MH-III is about 3.7 times larger than that reported for ice VII in [Fei et al. \(1993\)](#). Although, at 400 K this ratio reduces to about 1.06. Compared with the data reported by [Bezacier et al. \(2014a\)](#), the latter ratio is on average 1.16.

At lower pressure $\text{H}_2\text{O}-\text{CH}_4$ takes the form of a sI clathrate hydrate. The pure water ice polymorph in equilibrium with this phase is ice Ih. In the temperature range 100–250 K the sI clathrate hydrate to ice Ih volumetric thermal expansion ratio is in the range of 2–4 ([Hester et al. 2007](#); [Feistel & Wagner 2006](#)). Our results, therefore, represent a continuation of this trend to the high pressure MH-III structure as well.

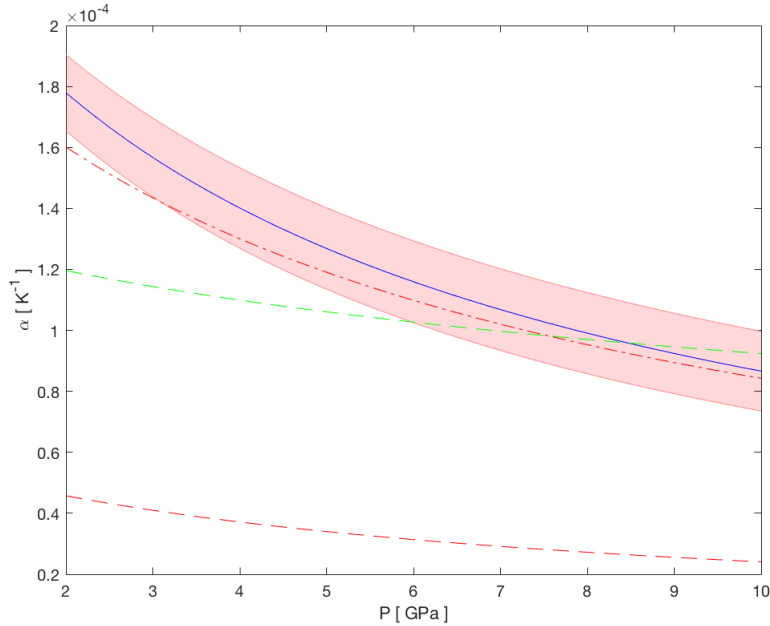


Figure 6. Volume thermal expansion coefficient versus pressure for: MH-III from this work (solid blue, shaded area is the 1σ error), water ice VII at 400 K from [Fei et al. \(1993\)](#) (dashed-dotted red), water ice VII at 300 K from [Fei et al. \(1993\)](#) (dashed red), and water ice VII from [Bezacier et al. \(2014a\)](#) (dashed green).

5. HEAT CAPACITY

In [Fig. 7](#) we plot the isochoric heat capacity per atom, normalized by Boltzmann’s constant. This normalization, and the comparison to the Dulong-Petit reference, provides a direct insight into the importance of quantum corrections to the nuclei dynamics in calculating the heat capacity. Clearly, for pure water ice polymorphs, our temperature range of interest is likely below the Debye temperature. If this is true for MH-III as well, then our classical MD treatment for the nuclei is inadequate for deriving the heat capacity. In this case, it is preferable to treat both electrons and nuclei quantum mechanically, as in [Benoit et al. \(1998\)](#). In this work we apply a quantum correction, using the harmonic oscillator approximation, to our classical MD as suggested by [Berens et al. \(1983\)](#). We derive the velocity autocorrelation function from our simulation, and its Fourier transform, i.e. the vibrational spectrum of the lattice, $g(\nu)$. The latter conforms with the normalization condition,

$$\int_0^\infty d\nu g(\nu) = 1 \quad (5)$$

The corrected heat capacity, for a system of N atoms and total mass M , is then given by,

$$C_v = 3k \frac{N}{M} \int_0^\infty g(\nu) \left(\frac{h\nu}{kT} \right)^2 \frac{e^{h\nu/kT}}{(e^{h\nu/kT} - 1)^2} d\nu \quad (6)$$

This approach shows good agreement with experimental data for the case of high-pressure ammonia ([Bethkenhagen et al. 2013](#)), in reproducing the equations of state for water ices VII and X ([French & Redmer 2015](#)), and in reproducing the heat capacity of methane ([Qi & Reed 2012](#)). The derived values, using this method, are also tabulated in [table 3](#). Our results indicate a low Debye temperature for MH-III.

In addition, we estimate the isochoric heat capacity by calculating the derivative of the internal energy with respect to temperature using the central finite difference scheme. For a finite central difference scheme the error depends on the third order derivative. We do not have enough data in order to estimate the latter derivative. Therefore, the error in the finite difference scheme is here estimated using the second order derivative, which is the error in the less accurate forward finite difference scheme. Thus, the error reported here is a maximal value. We further consider the error due to statistical errors in the simulated energy using block sampling. However, this error is lower than the former estimated error, except for the case of the atomic volume of $6.41 \text{ \AA}^3 \text{ atom}^{-1}$.

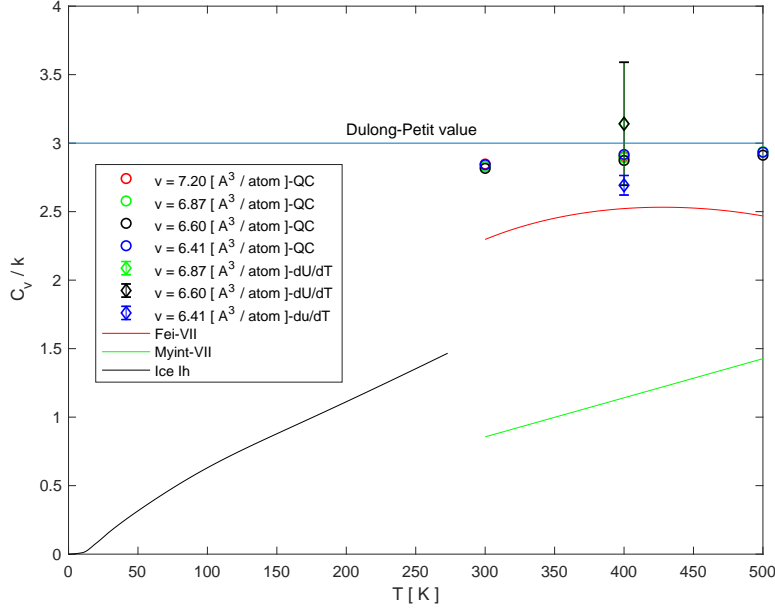


Figure 7. The isochoric heat capacity in terms of degrees of freedom (DOF) per atom versus temperature. Diamond data points and error bars are from the derivative of the internal energy with respect to the temperature (this work). Circle data points are after applying the quantum-mechanical correction using eq.6 (this work). Solid red curve is from data published in [Fei et al. \(1993\)](#) for ice VII. Solid green curve is from data published in [Myint et al. \(2017\)](#) for ice VII. Solid black curve is from data published in [Feistel & Wagner \(2006\)](#) for ice Ih.

Table 3. Normalized C_v of MH-III

V [Å ³ atom ⁻¹]	T [K]	C_v/k
7.20	300	2.85
	400	2.90
6.87	300	2.83
	400	2.90
	500	2.94
6.60	300	2.82
	400	2.87
	500	2.91
6.41	300	2.84
	400	2.92
	500	2.93

In studying planetary internal structure and formation the isobaric heat capacity is required. For MH-III we convert our derived isochoric heat capacity into isobaric using the thermodynamic relation:

$$C_p = C_v + \frac{\alpha^2 TV}{\tilde{\kappa}} \quad (7)$$

where the volume, V , coefficient of volumetric thermal expansion, α , and the compressibility, $\tilde{\kappa}$, were estimated in the previous section.

In Fig.8 we give our derived isobaric heat capacity as a function of pressure, for various isotherms. As for the case of ice VII, the isobaric heat capacity is relatively insensitive to the pressure. In Fig.9 we give the isobaric heat capacity

as a function of the temperature. For clarity, in table 4, we tabulate our derived isobaric heat capacity adopting the quantum harmonic approximation.

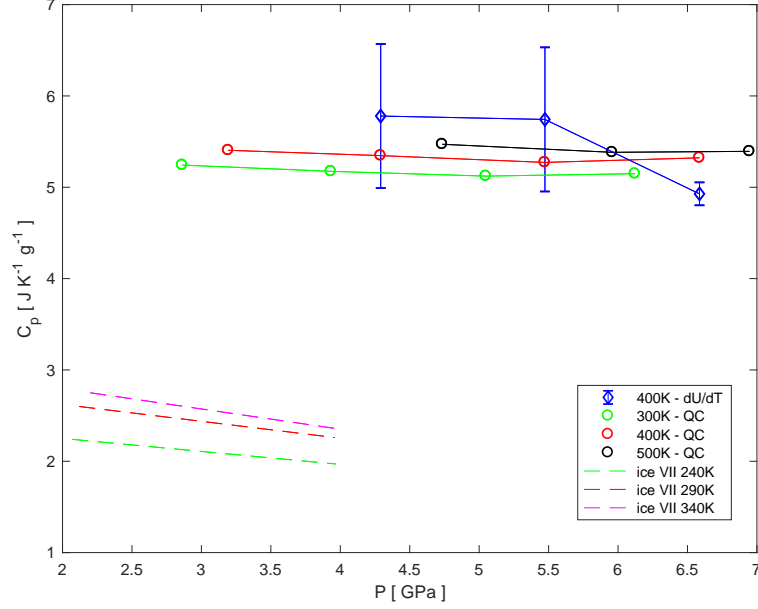


Figure 8. The isobaric heat capacity versus pressure, for various isotherms. Blue diamonds and accompanying errors are from the finite difference derivative of the internal energy (this work). Open circles are data points including the quantum correction (this work). Dashed curves are calculated isobaric heat capacity for ice VII from Tchijov (2004).

Table 4. C_p of MH-III

V [$\text{\AA}^3 \text{atom}^{-1}$]	T [K]	P [GPa]	C_p [$J g^{-1} K^{-1}$]
7.20	300	2.86	5.24
	400	3.19	5.40
6.87	300	3.93	5.17
	400	4.29	5.35
	500	4.73	5.47
6.60	300	5.05	5.12
	400	5.47	5.27
	500	5.96	5.38
6.41	300	6.12	5.14
	400	6.59	5.32
	500	6.95	5.39

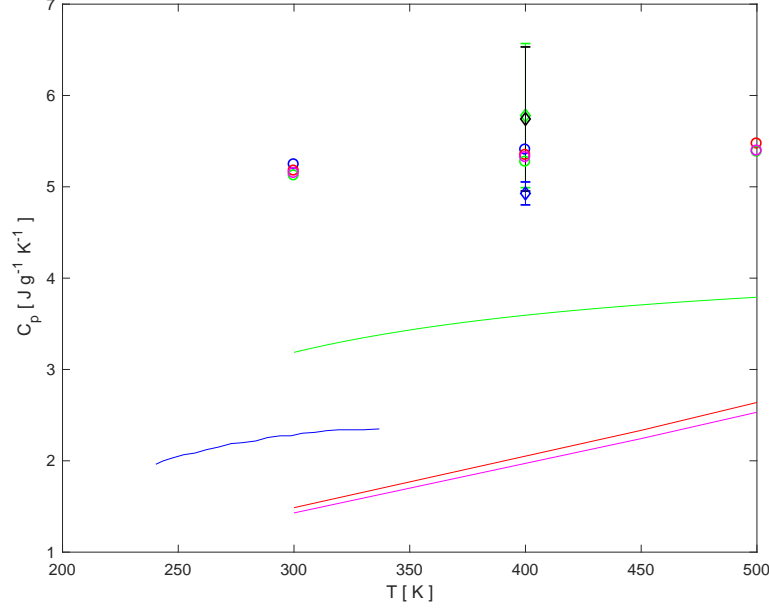


Figure 9. The isobaric heat capacity versus temperature. Diamonds and accompanying errors are from the finite difference derivative of the internal energy from this work: green ($v = 6.87 \text{ \AA}^3 \text{ atom}^{-1}$), black ($v = 6.60 \text{ \AA}^3 \text{ atom}^{-1}$) and blue ($v = 6.41 \text{ \AA}^3 \text{ atom}^{-1}$). Open circles are data points including the quantum correction (this work): blue ($v = 7.20 \text{ \AA}^3 \text{ atom}^{-1}$), red ($v = 6.87 \text{ \AA}^3 \text{ atom}^{-1}$), green ($v = 6.60 \text{ \AA}^3 \text{ atom}^{-1}$) and magenta ($v = 6.41 \text{ \AA}^3 \text{ atom}^{-1}$). Solid red and magenta curves are for ice VII from Myint et al. (2017), for $v = 6.41$ and $v = 6.60 \text{ \AA}^3 \text{ atom}^{-1}$, respectively. Solid blue curve is a calculated isobaric heat capacity for ice VII from Tchijov (2004). Solid green curve is the isobaric heat capacity for ice VII from Fei et al. (1993).

6. THE PHASE DIAGRAM

In Fig.10 we plot the phase diagram for the $\text{H}_2\text{O}-\text{CH}_4$ system, focusing on the likely dissociation curve for MH-III, in the interior of Titan and super-Titan moons.

Three experimental works have been published on the dissociation curve of MH-III with widely varying results (Kurnosov et al. 2006; Bezacier et al. 2014b; Kadobayashi et al. 2018). Bezacier et al. (2014b) report of a sample at 3.03 GPa and 395 K where ice VII melted while grains of MH-III remained stable in the liquid water. Therefore, both Kurnosov et al. (2006) and Bezacier et al. (2014b) agree that the thermodynamic stability field of MH-III extends to temperatures higher than the depressed melting temperature of high pressure water ice. However, these two works disagree over the range of this extended stability. Bezacier et al. (2014b) find that the dissociation curve of MH-III is quite close to the melting curve of pure high pressure water ice. However, Kurnosov et al. (2006) report that the dissociation curve of MH-III penetrates tens of degrees into the pure liquid water regime. The results of Kurnosov et al. (2006) thus imply that CH_4 stabilizes filled ice in a way that resembles its stabilizing effect in clathrate hydrates, the latter are known to be stable tens of degrees above the melting curve of water ice Ih. Contrary to previous works Kadobayashi et al. (2018) find that MH-III first separates into ice VII and solid CH_4 prior to melting. Another work, though yet unpublished, observed MH-III co-existing with liquid at 2.32 GPa and 370 K, about 7 K above the melting line of D_2O ice VII (Dominic Fortes, Personal Communication).

We note that Kurnosov et al. (2006) worked on the ternary $\text{H}_2\text{O}-\text{CH}_4-\text{NH}_3$ solution. It has been shown, both experimentally and theoretically, that molecules such as NH_3 and CH_3OH can increase the reactivity of water ice surfaces and act as catalysts to clathrate hydrate formation (Shin et al. 2012, 2013). This may be the reason for the more extended stability field for MH-III reported in Kurnosov et al. (2006). If this is indeed the case, then having 15 wt.% NH_3 in their solution suggests that the results of Kurnosov et al. (2006) are less directly applicable to the interior of Titan. This is because NH_3 was recently estimated to be only 2–3 wt.% relative to water in Titan’s interior (Tobie et al. 2012), in contradiction to earlier and higher estimates (Lunine & Stevenson 1987). The abundance of CH_3OH in the interior of Titan is not well constrained.

The temperature immediately above the rocky core is likely kept close to melting conditions (Choblet et al. 2017). Following the melting curve of ice VI, the pressure needed to form MH-III is at its lowest value, of approximately 1.5 GPa (see fig.10). Therefore, for a moment of inertia (MOI) of 0.34, it is not likely that MH-III plays a role in

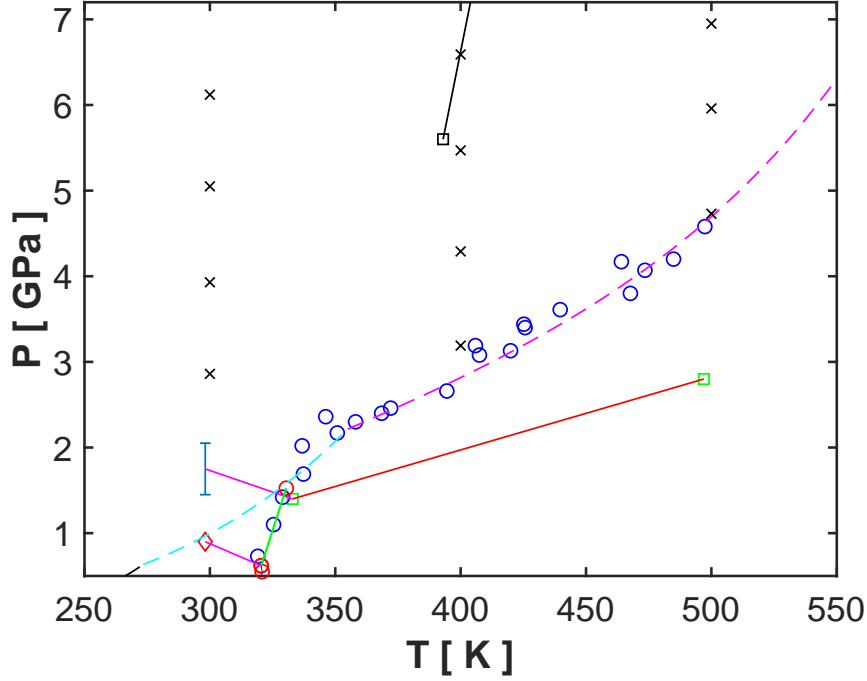


Figure 10. Phase diagram of the $\text{H}_2\text{O}-\text{CH}_4$ system. Dashed lines are the melting curves of pure water ice: ice VI (dashed cyan) and ice VII (dashed magenta). Solid green curve is the dissociation curve for sH CH_4 clathrate hydrate. Solid red (black) curve is the maximal (minimal) reported dissociation curve for MH-III. Blue circles are data points from [Bezacier et al. \(2014b\)](#) for the dissociation of MH-III and sH CH_4 clathrate hydrate. Solid magenta curves are: the transition from sI to sH (lower curve) and from sH to MH-III (upper curve). Red circles are data points from [Dyadin et al. \(1997\)](#). Green squares are data points from [Kurnosov et al. \(2006\)](#). Red diamond is a data point from [Loveday et al. \(2001a\)](#). Error bar encompasses the scatter in the reported data between [Loveday & Nelmes \(2008\)](#), [Loveday et al. \(2001a\)](#) and [Hirai et al. \(2001\)](#). This scatter in the data probably arises from the kinetic inhibition of the phase transition, and from the difficulty in interpreting the neutron diffraction patterns of phases that have disordered protons. Black square is a data point from [Kadobayashi et al. \(2018\)](#). Black crosses are the sampled points of this work.

contemporary Titan (see left panel in fig. 3). However, for an MOI of 0.33, and for our highest ocean density scenario, a pressure of 1.5 GPa is exceeded for $\rho_{\text{rock}} > 3.05 \text{ g cm}^{-3}$. Thus, in this case an undifferentiated ice-rock layer may partially occupy the thermodynamic regime where MH-III is stable.

For a rock density of 3.5 g cm^{-3} , and ocean density of 1.24 g cm^{-3} , an MH-III enriched sublayer would span a pressure range of approximately 0.35 GPa (thickness of 130 km) above the rocky core. If half of the mass of this sublayer is rock, and because the mole ratio of H_2O to CH_4 in MH-III is 2 : 1, then this layer is capable of storing about 7×10^{22} mol of CH_4 , which is about 10^{24} g of CH_4 . This is about $3000\times$ the CH_4 inventory estimated in Titan’s surface and atmosphere ([Lorenz et al. 2008](#); [Niemann et al. 2010](#)), and represents about 40% of the carbon content in Titan’s interior (see table 2 in [Tobie et al. 2012](#)). Earlier work estimated the total mass of CH_4 accreted into Titan’s core to be 10^{23} g, assuming a hot accretion, and 10^{24} g, assuming a cold accretion ([Lunine & Stevenson 1987](#)). Clearly, MH-III is capable of storing a substantial part, if not the lion’s share, of the core accreted CH_4 , possibly hindering its outgassing into the atmosphere. Whether this is the case depends on the stability and thermal evolution of this sublayer which is dealt with in the next section.

7. THERMAL EVOLUTION AND THE MH-III LAYER

In this section we quantify the effects a layer enriched in MH-III would have on the thermal evolution of the interior, and consequently on the stability of this layer. We estimate the role of MH-III as a possible CH_4 reservoir through time. Again, we will use Titan as an end member test case for our studied worlds. MH-III is a high-pressure ice structure, which if found in the interior, is likely overlying the rocky core. Thus, it is important to first calculate the heat flux out of the core.

As in [Grasset et al. \(2000\)](#) we assume an initial temperature of 500 K for the core, following core overturn. At this stage the high viscosity hinders convective motion and heat is transported conductively ([Grasset et al. 2000](#)). The solution for the conductive profile in the rocky core appears in the appendix. This solution is used here to calculate

the Rayleigh number for an internally heated core prior to the onset of convection. The appropriate Rayleigh number is (Schubert et al. 2001),

$$Ra_{core} = \frac{\alpha_c \rho_c g_c H_c d_c^5}{C p_c \kappa_c \mu_c} \quad (8)$$

where $\kappa_c = 7 \times 10^{-3} \text{ cm}^2 \text{ s}^{-1}$ is the thermal diffusivity of rock (Yomogida & Matsui 1983), $C p_c = 9.2 \times 10^6 \text{ erg g}^{-1} \text{ K}^{-1}$ is the heat capacity of rock (Yomogida & Matsui 1983), $\rho_c = 3.5 \text{ g cm}^{-3}$ is our assumed rock density. This corresponds to a rock thermal conductivity of $2.25 \times 10^5 \text{ erg s}^{-1} \text{ K}^{-1} \text{ cm}^{-1}$. The rock thermal expansivity coefficient $\alpha_c = 2.4 \times 10^{-5} \text{ K}^{-1}$ is taken from Kirk & Stevenson (1987) based on ultramafic rocks. The dynamic viscosity for the core, μ_c , is here also adopted from Kirk & Stevenson (1987). For the highest ocean density we have solved for and for our choice for the rock density the core radius is $d_c = 1442 \text{ km}$. g_c is the acceleration of gravity at mid-core. H_c is the radiogenic heat production rate per unit mass which is adopted from Grasset et al. (2000).

Properly scaling the radiogenic heat budget requires the timescale for the core overturn to complete, which as in Grasset et al. (2000) we denote as t_0 . Lunine & Stevenson (1987) found $t_0 \sim 1 \text{ Gyr}$. As is seen from the phase diagram the presence of MH-III in the undifferentiated rocky core may require higher temperatures in order to achieve melting and core overturn. An upward shift of about 100 K in the melting temperature (according to Kurnosov et al. 2006), relative to pure water ice, would increase t_0 by 100 Myr. We will not consider this effect here due to uncertainties in the initial temperature for the core and the relatively small change to t_0 . Finally, the onset of convection in the rocky core is when the Rayleigh number reaches a critical value here estimated to be 2000, though this value depends on the boundary conditions (see subsection 7.5 in Schubert et al. 2001).

If the mole ratio of H_2O to CH_4 is higher than 2 : 1, then any excess water would form ice VI after all CH_4 was incorporated into MH-III. The melting temperature of ice VI is likely lower than that for MH-III. Therefore, by being the first phase to melt, and advect excess heat, it is reasonable that the outer boundary temperature for the rocky core is set at the melting temperature of ice VI (here 342 K).

With these assumptions we find that the onset of convection in the core is at $t_{oc} = t_0 + 1.34 \text{ Gyr}$. In Fig. 11 we plot the heat flux out of the core, and into a possible MH-III enriched layer, prior to the onset of convection in the core. The scaled radiogenic heat flux is higher than the actual flux indicating a heating stage for the core. We further give in Fig. 11 the conductive temperature profile in the core at the onset of convection. The high temperature ($\approx 1200 \text{ K}$) will not allow for the survival of MH-III in the inner core at this stage.

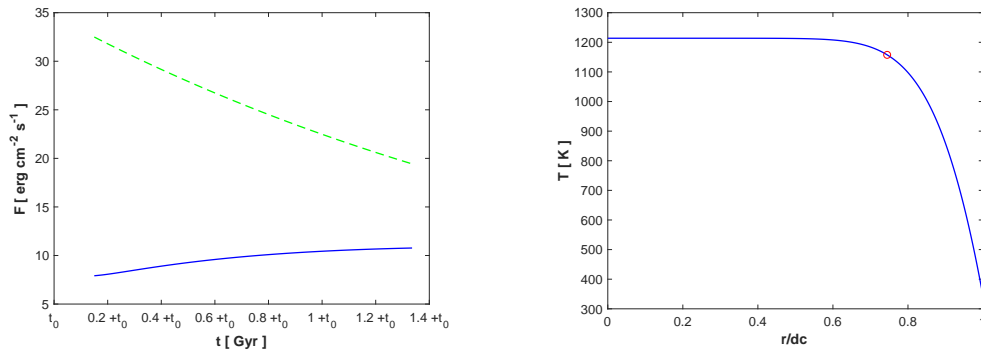


Figure 11. (left panel) Heat flux out of the core and into the MH-III enriched layer prior to the onset of convection within the core (solid blue curve). Dashed-dotted (green) is the radiogenic budget scaled to the outer core surface. **(right panel)** Conductive thermal profile in the core at the onset of convection. Red circle is the base of the forming stagnant lid.

The large temperature gradient in the core, at the onset of convection, corresponds to a very large viscosity contrast (50 orders of magnitude). Therefore, a stagnant lid forms, confining convection to the inner part of the rocky core. The temperature difference driving convection in this case is proportional to the rheological temperature (Solomatov 1995). Davaille & Jaupart (1993, 1994) found the following form for this temperature difference,

$$\Delta T = -a_{rh} \frac{\mu_c(T_c)}{\left(\frac{d\mu_c}{dT}\right)_{T_c}} \quad (9)$$

where T_c is the convection cell temperature, and $a_{rh} = 2.24$. Reese et al. (2005) fit their numerical simulations for internally-heated spherical shells to scaling laws with an averaged $a_{rh} = 3.2$. Thiriet et al. (2019) have shown that 1-D parameterized models for the heat transport can well reproduce data from 3-D thermal evolution models for the stagnant lid regime. They suggest a best fit for a_{rh} of 2.54.

By subtracting ΔT from the mid-core temperature we can determine the temperature at the base of the stagnant lid and its thickness, d_{sl} , at the onset of convection. We solve for the a_{rh} values suggested above (see table 5). For all cases the initial temperature of the convection cell is 1214 K.

Table 5. Thickness of the stagnant lid at the onset of convection.

a_{rh}	$d_{sl}(\text{VI})$ [km]
2.24	381
2.54	368
3.2	344

In order to derive the heat flux into a possible MH-III enriched layer following the onset of convection in the rocky core we adopt the 1-D model from Thiriet et al. (2019). The rocky core is divided into three layers, the convection cell, a cold boundary (i.e. the rheological layer), and a stagnant lid. The difference between the heat provided by the convecting core, via the cold boundary layer, and the heat conducted away at the base of the lid yields the stagnant lid evolution with time. The convective heat flow is estimated using the Nusselt number which scales as the Rayleigh number to the power of β . In this work we adopt the best-fit value of $\beta = 0.335$ (Thiriet et al. 2019). Also as in Thiriet et al. (2019) we use a fourth-order Runge-Kutta scheme to advance the convection cell temperature, T_c , and the thickness of the stagnant lid with time. We solve numerically for the heat conduction within the stagnant lid using an implicit scheme and cartesian coordinates, with 100 spatial levels. The initial set up is the stagnant lid thickness and convection cell temperature at the onset of convection, given above. The initial temperature profile along the stagnant lid is derived using the analytical solution given in the appendix.

In Fig.12 we give the evolution with time of the average temperature of the convective part of the rocky core, and of the stagnant lid thickness for the various parameter options from table 5. The projection into the future is a test for a well behaving numerical solution. Fig.13 is the heat flux, following the onset of convection, out of the rocky core and into a possible overlying MH-III enriched layer. Our derived heat flux is not sensitive to the choice for a_{rh} .

In Fig.14 we plot the thermal profile in the stagnant lid and in the mixed ice-rock layer on-top of the $\text{H}_2\text{O}-\text{CH}_4$ phase diagram (thick blue curves). Two possibilities emerge for the survival of MH-III, one within the outer part of the rocky core and the other is within the mixed ice-rock layer.

In addition to the mixed ice-rock layer, and depending on the location of the melting curve of MH-III, it is possible that MH-III survived in a thin layer within the outer part of the rocky core to the present. This though may depend on local concentrations of NH_3 and CH_3OH . The extent of such a layer depends on the core temperature, and thus the radiogenic budget. For our calculation this layer is 12 km wide. For the lower core temperature (≈ 1000 K) from Grindrod et al. (2008) this layer is 39 km wide. Assuming the volume fraction of MH-III in this layer varies between 1 – 10%, we find this layer can hold $7 \times 10^{19} - 7 \times 10^{20}$ mol of CH_4 . This is equivalent to 3 – 30 \times the surface and atmospheric budget of CH_4 (Lorenz et al. 2008; Niemann et al. 2010). For the lower core temperature of Grindrod et al.

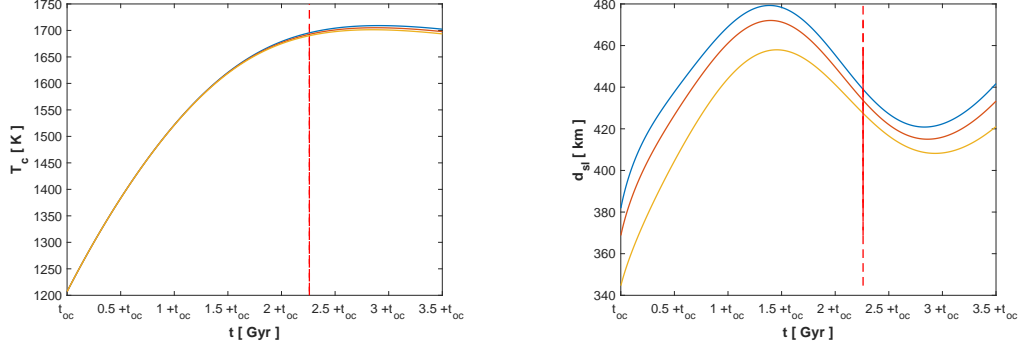


Figure 12. (left panel) Temporal evolution of the convection cell temperature in the rocky core, from the onset of convection to the present (the vertical red dashed line marks the present) and projected ≈ 1 Gyr into the future. (right panel) Temporal evolution of the rocky core stagnant lid thickness, from the onset of convection to the present (the vertical red dashed line marks the present) and projected ≈ 1 Gyr into the future. Solid blue, red and yellow curves are for a_{rh} of 2.24, 2.54 and 3.20, respectively.

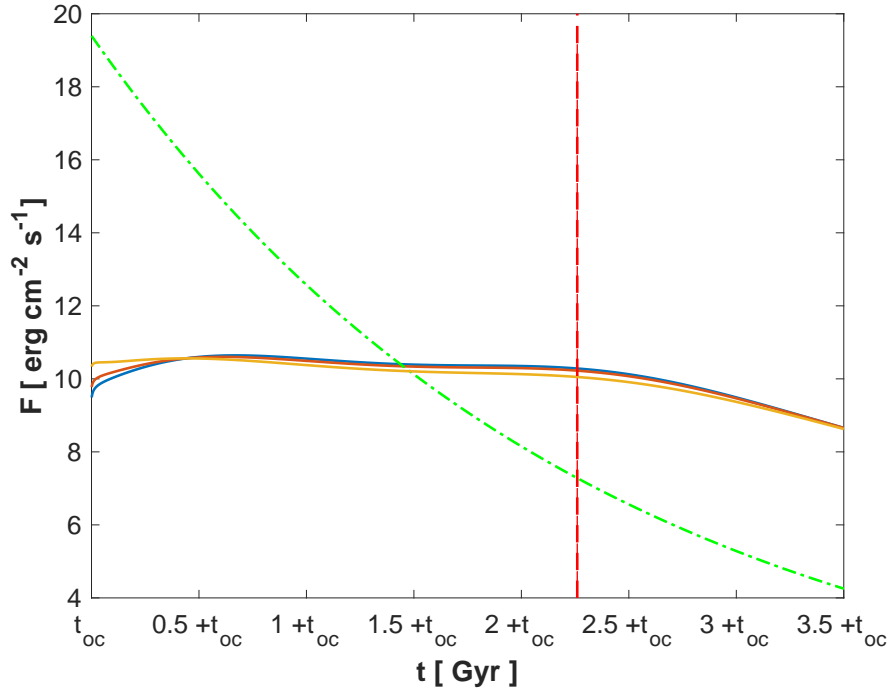


Figure 13. Temporal evolution of the heat flux out of the convective rocky core and into the mixed ice and rock layer, from the onset of convection to the present (the vertical red dashed line marks the present) and projected ≈ 1 Gyr into the future. Dashed-dotted (green) curve is the radiogenic budget scaled to the outer core surface.

(2008) this reservoir is equivalent to 9 – 90 \times the surface and atmospheric budget of CH $_4$. If the melting temperature

of MH-III is closer to that reported by [Bezacier et al. \(2014b\)](#) then this reservoir is likely negligible, hence leaving MH-III as a possible CH_4 reservoir only within the mixed ice-rock layer.

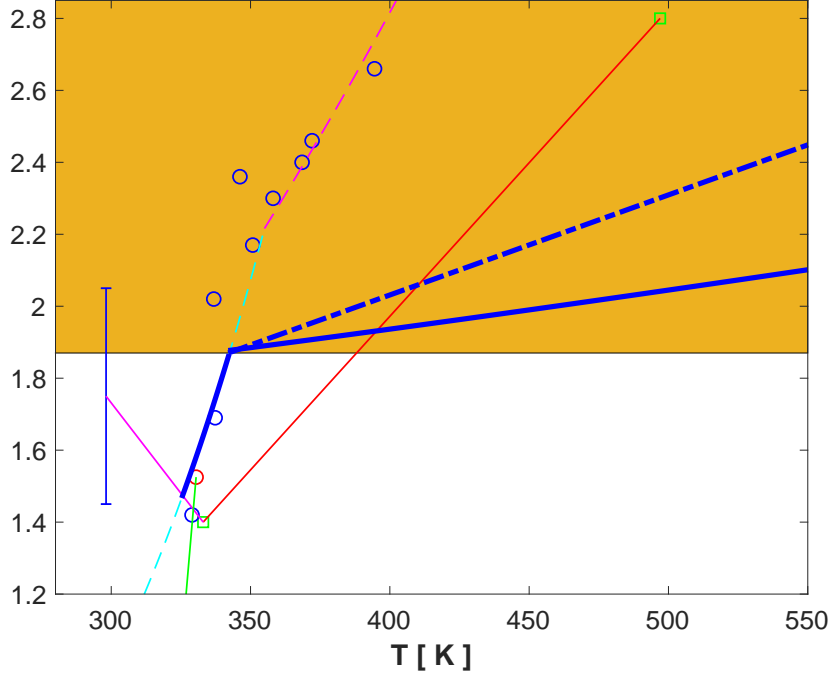


Figure 14. The thermal profile in the outer part of the core stagnant lid and within the thermodynamic stability field of MH-III in the mixed ice-rock layer. Our derivation for present day Titan (thick solid blue), and for the lower internal temperature in the core from [Grindrod et al. \(2008\)](#) (thick dashed blue). Shaded area represents the rocky core. The reader is referred to Fig.10 for a list of all other symbols in the plot.

In order to estimate the mode of heat transport across the mixed ice-rock layer we note that the high-pressure ice cold boundary layer (i.e. high-pressure ice to subterranean ocean interface, see Fig.1) is confined to the melting curve of high-pressure ice ([Choblet et al. 2017](#)). The melting curve of ice V has a gradient of approximately 60 K GPa^{-1} . Adopting the thermal conductivity for ice VI from [Chen et al. \(2011\)](#) yields a flux of $0.2 \text{ erg cm}^{-2} \text{ s}^{-1}$. The latter value is far less than our estimated heat flux out of the core. Therefore, melting of ice is a prominent mode of heat transport, as reported by [Choblet et al. \(2017\)](#) and [Kalousová et al. \(2018\)](#), both during the conductive and convective phase of the core. Thus, it is likely that the thermal profile in the ice-rock layer above the core follows the melting curve of ice VI, the phase with the lowest melting temperature (see thick blue curve in Fig.14). Hence, the stability field of MH-III spans about 0.4 GPa above the core for our case of study, which as stated in the previous section, suggests this phase may be a major reservoir for CH_4 .

For melting to be an efficient coolant it ought promote positively buoyant hot plumes. The density of ice VI is indeed higher than that of liquid water, promoting buoyancy and melt extraction. In order to consider the effect of MH-III we plot in Fig.15 the density difference between that for pure liquid water (taken from [Wagner & Pruss \(2002\)](#)) and for MH-III (derived in this work). Liquid water is denser than MH-III for the P-T conditions of interest for modeling Titan and possibly for super-Titans as well. This was observed experimentally at 3.03 GPa and 395 K, where ice VII melted while the grains of MH-III migrated to the upper part of the vessel where the sample was held ([Bezacier et al. 2014b](#)).

In a water-rich system (if $\text{H}_2\text{O}:\text{CH}_4$ mole ratio $>2:1$) both ice VI and MH-III would form, or ice VII and MH-III, depending on the pressure. Because ice VI likely has a lower melting temperature than MH-III, then melting on the outer surface of the rocky core would tend to aggregate solid MH-III on top of the melt, consequently hindering the formation of hot positively buoyant plumes. In this case the melt would further increase in temperature until it becomes positively buoyant. In Fig.16 we plot the excess temperature (temperature above the melting temperature of pure high-pressure water ice) required in order for liquid water to become positively buoyant relative to a MH-III and rock, and MH-III and pure high-pressure ice (VI or VII), composition. The density of ice VI and VII near their

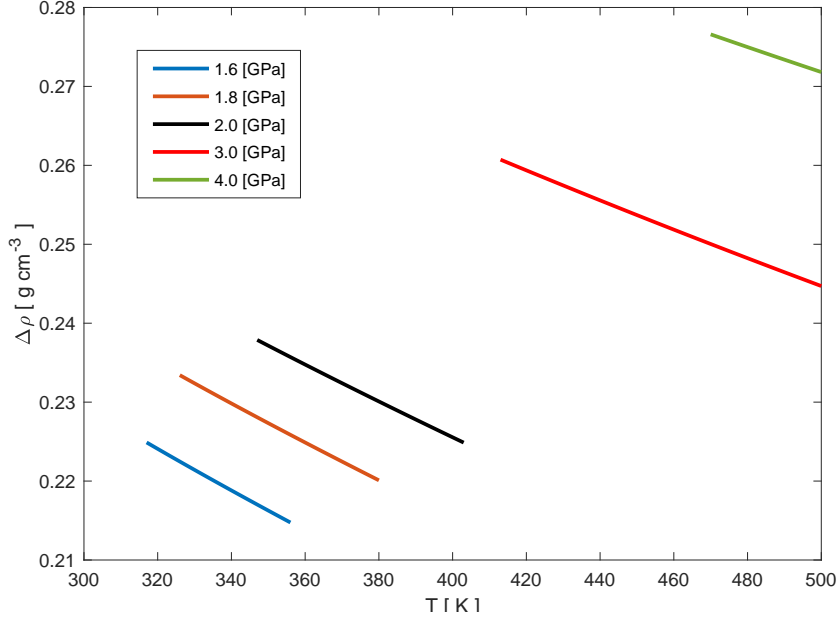


Figure 15. The difference in density between pure liquid water (from [Wagner & Pruss \(2002\)](#)) and MH-III (this work), for various isobars spanning part of the thermodynamic stability field of MH-III.

melting curve is taken from [Bezacier et al. \(2014a\)](#) and [Frank et al. \(2004\)](#).

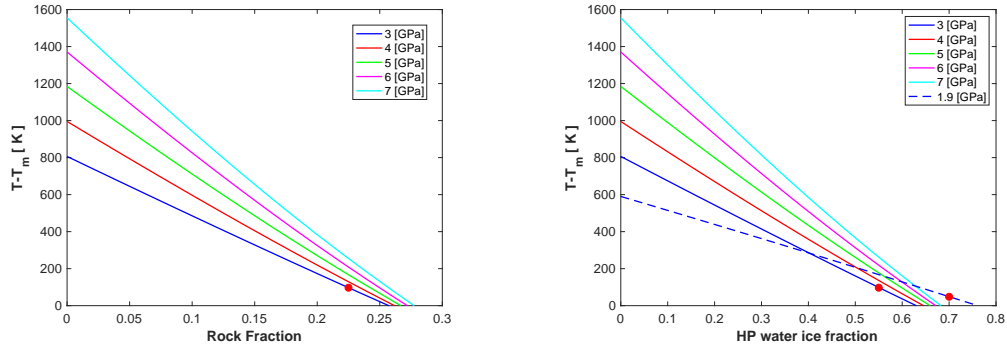


Figure 16. (left panel) Excess temperature, above the melting point, needed to make liquid water positively buoyant relative to a mixture of MH-III and rock ($\rho_{rock} = 3.5 \text{ g cm}^{-3}$). Solved for various isobars. (right panel) Excess temperature, above the melting point, needed to make liquid water positively buoyant relative to a mixture of MH-III and high-pressure water ice (dashed curve for ice VI, solid curves for ice VII). Solved for various isobars. Red dots mark the upper boundary reported for the stability field of MH-III by [Kurnosov et al. \(2006\)](#).

If the mass fraction of rock ($\rho_{rock} = 3.5 \text{ g cm}^{-3}$) is higher than ≈ 0.3 , then the melt is always positively buoyant. If

rock is replaced with ice VII (more likely for super-Titans), then this threshold increases to ≈ 0.65 , and to ≈ 0.75 for the case of ice VI. Therefore, the mode of transport of CH_4 across an MH-III enriched layer becomes dependent on the composition of the layer. If the composition is such that the melt is always positively buoyant, then the upwelling melt would carry the fraction of CH_4 which can dissolve within the melt. However, if the composition of the layer is such that the melt experiences excess heating in order to become buoyant, then during its upwelling it may dissociate MH-III that it comes in contact with, thus carrying not only the dissolved fraction of CH_4 , but also CH_4 as a separate phase. For example, if the rock mass fraction is higher than 0.26, or possibly 0.22, (see 3 GPa isobar) then MH-III in the path of a hot plume may be stable, and CH_4 migrates as a dissolved component. However, if the mass fraction of rock is less than 0.22, then the excess temperature of the melt would also dissociate MH-III along its path. The latter value would become closer to 0.26 for the dissociation conditions of MH-III reported by [Bezacier et al. \(2014b\)](#). For the case of super-Titans, if the mass fraction of ice VII is less than ~ 0.5 , hot plumes at the core boundary would dissociate MH-III causing rapid outward migration of CH_4 , perhaps into the atmosphere.

8. DISCUSSION

MH-III is an important phase within the $\text{H}_2\text{O}-\text{CH}_4$ binary system that should be considered when modeling water-rich bodies. Its thermodynamic stability field is very wide, overlapping those of ice VI, VII and X. In addition it has a high capacity for storing CH_4 ($\text{H}_2\text{O}:\text{CH}_4$ mole ratio of 2:1). We show that MH-III may exist in the interior of Titan for part of the parameter space describing Titan’s inferred internal structure. However, this phase is likely dominant in the interior of super-Titans owing to the higher pressures reached within their water-rich ice mantles. This has two interesting consequences, (1) it may further constrain Titan’s interior models, (2) it may create a dichotomy breaking analogies between Titan and super-Titans.

We describe two modes for the outward transport of CH_4 across a MH-III enriched layer, either as a dissolved component within a buoyant melt, or largely as a separate phase (in addition to partially dissolved) if the melt is of a high enough temperature to dissociate MH-III in its path. These two modes represent different CH_4 transport efficiencies if the solubility value is low. The solubility of CH_4 when in equilibrium with MH-III is not known. If it is low, and dissolution of CH_4 is the prime mode of transport, then melt extraction may not be an efficient mechanism for the outward transport of CH_4 out of an MH-III enriched layer. In this case the abundant presence of CH_4 at the surface and atmosphere of Titan makes a high moment of inertia (0.34) more likely, since MH-III will not be stable in Titan’s interior in this case. Another possibility is that the composition of the ice-rock mixed layer, assumed in our model, is poor in rock ($\lesssim 0.2$ in mass fraction) resulting in a buoyant melt that is hot enough to dissociate MH-III along its path.

In [Levi et al. \(2014\)](#) we have suggested that the presence of MH-III would shift adiabatic thermal profiles to higher temperatures when compared against adiabats in ice VII. Our new results for the volume thermal expansivity and isobaric heat capacity for MH-III confirm this earlier estimation which was not based on ab initio models for MH-III (see Fig.17). This shift to higher temperatures ought affect the dynamics of ice mantles, and couple between dynamics and composition along the history of CH_4 transport and outgassing. However, such an analysis would require a better understanding of the viscosity of high-pressure solid solutions.

The interiors of the icy moons of our solar system reach relatively low pressures. The highest pressure inside Titan is only about 6 GPa. Their total mass of volatiles is also likely small in comparison to what is stored inside a ice-rich planet or a super-Moon. Therefore, the high capacity of MH-III for storing volatiles makes it important, even if it is only stabilized over a narrow pressure range (~ 0.1 GPa).

Observations beyond our solar system may detect super-Titans down to twice the mass of Mars ([Kipping et al. 2009](#); [Heller 2014](#)). [Heller & Pudritz \(2015a,b\)](#) have shown that super-Titans and super-Ganymedes can form in the accretion disks around super-Jovian planets, noting that hot Jupiters have already been detected.

Polymorphs of filled ice likely play a major role in the transport and outgassing of volatiles for the case of the more massive super-Titans and water worlds. Filled ices form not just in the $\text{H}_2\text{O}-\text{CH}_4$ system (i.e. MH-III) but also in the $\text{H}_2\text{O}-\text{CO}_2$ and $\text{H}_2\text{O}-\text{N}_2$ systems ([Loveday & Nelmes 2008](#)). Thus, separating between biotic and abiotic atmospheric signatures requires a better understanding of these phases and their thermophysical nature. We hope that the community of high-pressure experimentalists and computational material scientists would invest more resources in the study of filled-ices. Such knowledge for the lower pressure clathrate hydrates yielded a general framework for modeling multi-component systems. It is time to do the same for filled-ices if we wish to realistically constrain the uncertainty of biosignatures in water worlds.

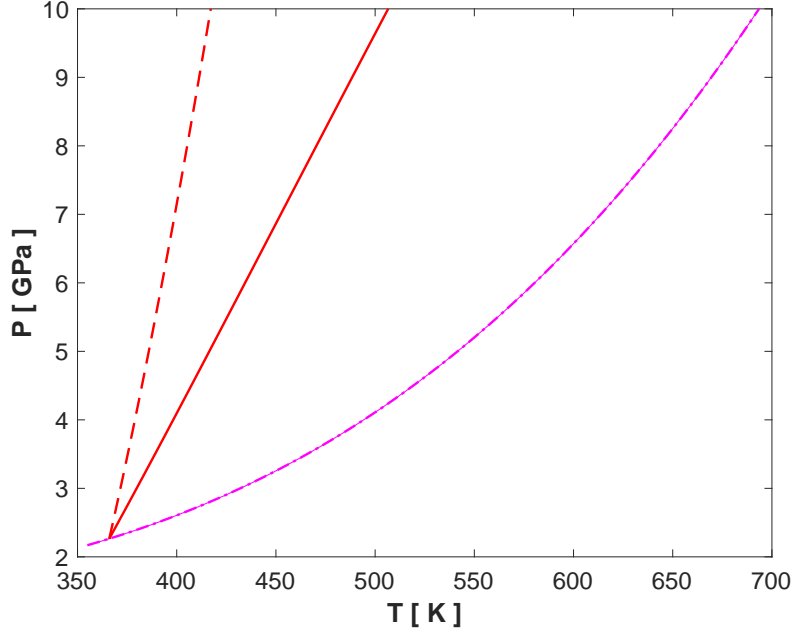


Figure 17. Adiabatic profiles assuming a composition of ice VII (dashed red), and a composition of MH-III (solid red). Dashed-dotted (magenta) is the melting curve of ice VII from [Lin et al. \(2004\)](#).

9. SUMMARY

CH_4 is an important biosignature. Therefore, studying its potential internal reservoirs and abiotic origins is needed. MH-III (CH_4 filled-ice Ih) is a phase that forms in the H_2O - CH_4 binary mixture above about 1.5 GPa, depending on the temperature (see Fig.10). In this work we calculate the thermal equation of state and heat capacity of MH-III in the temperature range of 300 K-500 K and pressure between 2 GPa-7 GPa, using first-principles electronic structure methods. These temperature and pressure regimes are adequate for studying the role of MH-III as a possible reservoir for CH_4 in Titan and supr-Titan class objects, speculated to be potentially habitable. This paper focuses on Titan, an endmember in this family of objects.

We assume for Titan a layered model consisting of a mixed ice-rock layer above a rocky core and underlying a high-pressure ice layer, topped by a subterranean ocean and a crust (see Fig.1). Using observational constraints for Titan we derive the thickness of the different layers as a function of ocean and rock mass density. We show that for a normalized moment of inertia (MOI) of 0.34 the highest pressure on the outer boundary of the rock core is less than 1.5 GPa, hence not allowing for the formation of MH-III. However, for a MOI of 0.33, and an ocean density of 1.24 g cm^{-3} , MH-III may form above the rocky core if the rock density is higher than 3.05 g cm^{-3} . In this case a layer, about 100 km thick, may form above the rocky core that falls inside the thermodynamic stability field of MH-III. Since the mole ratio of $\text{H}_2\text{O}:\text{CH}_4$ in MH-III is 2:1 this is potentially a large reservoir for CH_4 ($\sim 3000\times$ the surface and atmospheric inventory of CH_4 for the case of Titan).

We use a 1-D thermal evolution model to calculate the heat flux out of Titan's rocky core and into a possible MH-III enriched layer. The heat flux out of the core is $\approx 10 \text{ erg cm}^{-2} \text{ s}^{-1}$. We show that internal core temperatures are high enough so as to dissociate MH-III out of the core. An exception is a thin ($\approx 10 \text{ km}$) layer on the outer core where MH-III may survive to the present between rock grains, likely not holding more than 10^{20} mol of CH_4 (assuming a 1% porosity). We corroborate, as previously shown by [Choblet et al. \(2017\)](#) and [Kalousová et al. \(2018\)](#), that melting and melt migration is an important heat transfer mechanism above the rocky core. However, our derived equation of state for MH-III shows it is less dense than liquid water, consequently hindering melt extraction. Melt may need to be further heated to temperatures above the melting temperature in order to become positively buoyant.

For the case of a mixed MH-III and rock layer, a rock mass fraction higher than 0.3 would turn melt positively

buoyant upon melting. In this case the outward migration of CH_4 is likely in the form of a dissolved component within the melt. For low rock mass fractions ($\lesssim 0.2$) the melt, upon reaching positive buoyancy, should be hot enough to dissociate MH-III along its path, thus transporting CH_4 outward more efficiently.

Water ice VII is a likely polymorph in the interior of super-Titans. Melt at the rock-ice mantle boundary for these larger objects should be positively buoyant upon melting if the mass fraction of ice VII is larger than 0.65 (mole ratio of $\text{H}_2\text{O}:\text{CH}_4$ larger than 5.5). In this case CH_4 likely migrates as a dissolved component within the melt. If, on the other hand, water is less abundant, then positively hot plumes are likely hot enough to dissociate MH-III as they migrate upward, yielding a faster depletion, and potentially outgassing, of internal CH_4 .

We calculate the heat capacity for MH-III, and show that it likely has a lower Debye temperature compared to pure water ice polymorphs. Together with our derived thermal expansivity coefficient we can calculate adiabats in the interior of super-Titans. We confirm an earlier suggestion made in [Levi et al. \(2014\)](#) that MH-III supports higher internal adiabatic temperature profiles.

10. ACKNOWLEDGEMENTS

We wish to thank our referee for important suggestions on how to improve the text.

AL is supported by a grant from the Simons Foundation (SCOL #290360 to D.S.). The computations in this paper were run on the Odyssey cluster supported by the FAS Division of Science, Research Computing Group at Harvard University. AL is grateful to the administrative staff for their technical support.

REC was supported by the European Research Council Advanced Grant ToMCaT and by the Carnegie Institution for Science. We gratefully acknowledge the Gauss Centre for Supercomputing e.V. (www.gauss-centre.eu) for funding this project in part by providing computing time on the GCS Supercomputer SuperMUC at Leibniz Supercomputing Centre (LRZ, www.lrz.de).

11. APPENDIX

11.1. Heat Conduction in a Heated Layer

Heat conduction in 1D with a time-dependent radiogenic heat source may be described with the following differential equation:

$$\kappa \frac{\partial^2 T}{\partial x^2} = -\frac{H_{cf}}{C_p} e^{-t/\tau} + \frac{\partial T}{\partial t} \quad (10)$$

where κ is the thermal diffusivity coefficient, T is temperature, H_{cf} is the radioactive heat production rate per unit mass at $t = 0$, C_p is the isobaric heat capacity, and τ is an averaged half-life for radioactive decay. Assuming a constant and uniform initial temperature of T_0 , the Laplace transform of the diffusion equation is:

$$\kappa \frac{d^2 \tilde{T}}{dx^2} - p \tilde{T} + \frac{H_{cf}}{C_p} \frac{1}{p + 1/\tau} + T_0 = 0 \quad (11)$$

where p is the frequency parameter. The general solution of the last equation is:

$$\tilde{T}(x, p) = A e^{\sqrt{p/\kappa} x} + B e^{-\sqrt{p/\kappa} x} + \frac{T_0}{p} + \frac{H_{cf}}{C_p} \frac{1}{p(p + 1/\tau)} \quad (12)$$

We consider a zero flux boundary at $x = 0$, and a constant temperature at the boundary $x = d_c$,

$$\frac{\partial T}{\partial x} \Big|_{x=0} = 0 \quad (13)$$

$$T \Big|_{x=d_c} = T_m \quad (14)$$

the Laplace transform of the boundary conditions is,

$$\frac{d\tilde{T}}{dx} \Big|_{x=0} = 0 \quad (15)$$

$$\tilde{T} \Big|_{x=d_c} = \frac{T_m}{p} \quad (16)$$

giving after a few algebraic steps the solution,

$$\tilde{T}(x, p) = \left(\frac{T_m - T_0}{p} - \frac{H_{cf}}{C_p} \frac{1}{p(p + 1/\tau)} \right) \frac{\cosh(qx)}{\cosh(qd_c)} + \frac{T_0}{p} + \frac{H_{cf}}{C_p} \frac{1}{p(p + 1/\tau)} \quad (17)$$

where $q \equiv \sqrt{p/\kappa}$. The last equation has poles at $p = 0$, $p = -1/\tau$, and for $\cosh(qd_c) = 0$. Using the inversion theorem we obtain the following solution,

$$T(x, t) = T_m - \frac{4(T_m - T_0)}{\pi} \sum_{n=0}^{\infty} \frac{(-1)^n}{2n+1} e^{-\kappa\gamma_n^2 t} \cos(\gamma_n x) - \frac{H_{cf}}{C_p} \left\{ \tau e^{-t/\tau} \left[1 - \frac{\cos(x/\sqrt{\kappa\tau})}{\cos(d_c/\sqrt{\kappa\tau})} \right] + \sum_{n=0}^{\infty} \frac{4(-1)^{n+1}}{\pi(2n+1) \left[\frac{1}{\tau} - \kappa\gamma_n^2 \right]} e^{-\kappa\gamma_n^2 t} \cos(\gamma_n x) \right\}$$

where,

$$\gamma_n \equiv \frac{(2n+1)\pi}{2d_c} \quad (18)$$

REFERENCES

- Baland, R.-M., Tobie, G., Lefvre, A., & Hoolst, T. V. 2014, *Icarus*, 237, 29
- Barr, A. C., Citron, R. I., & Canup, R. M. 2010, *Icarus*, 209, 858
- Baumert, J., Gutt, C., Krisch, M., et al. 2005, *Phys. Rev. B*, 72, 054302
- Benoit, M., Marx, D., & Parrinello, M. 1998, *Nature*, 392, 258
- Berens, P. H., Mackay, D. H. J., White, G. M., & Wilson, K. R. 1983, *The Journal of Chemical Physics*, 79, 2375
- Bethkenhagen, M., French, M., & Redmer, R. 2013, *The Journal of Chemical Physics*, 138, 234504
- Bezacier, L., Journaux, B., Perrillat, J.-P., et al. 2014a, *The Journal of Chemical Physics*, 141, doi:http://dx.doi.org/10.1063/1.4894421
- Bezacier, L., Menn, E. L., Grasset, O., et al. 2014b, *Physics of the Earth and Planetary Interiors*, 229, 144
- Brand, H. E. A., Fortes, A. D., Wood, I. G., & Vočadlo, L. 2010, *Physics and Chemistry of Minerals*, 37, 265
- Bussi, G., Donadio, D., & Parrinello, M. 2007, *The Journal of Chemical Physics*, 126, 014101
- Castillo-Rogez, J. C., & Lunine, J. I. 2010, *Geophysical Research Letters*, 37, doi:10.1029/2010GL044398
- Chen, B., Hsieh, W.-P., Cahill, D. G., Trinkle, D. R., & Li, J. 2011, *Phys. Rev. B*, 83, 132301
- Choblet, G., Tobie, G., Sotin, C., Kalousov, K., & Grasset, O. 2017, *Icarus*, 285, 252
- Consolmagno SJ, G. J., Macke SJ, R. J., Rochette, P., Britt, D. T., & Gattacceca, J. 2006, *Meteoritics & Planetary Science*, 41, 331
- Davaille, A., & Jaupart, C. 1993, *Journal of Fluid Mechanics*, 253, 1417166
- . 1994, *Journal of Geophysical Research: Solid Earth*, 99, 19853
- Dyadin, Y. A., Aladko, E. Y., & Larionov, E. G. 1997, *Mendelev Comm.*
- Fei, Y., Mao, H.-K., & Hemley, R. J. 1993, *J. Chem. Phys.*, 99, 5369
- Feistel, R., & Wagner, W. 2006, *J.Phys.Chem.Ref.Data*, 35, 1021
- Fortes, A. 2012, *Planetary and Space Science*, 60, 10, titan Through Time: A Workshop on Titans Formation, Evolution and Fate
- Frank, M. R., Fei, Y., & Hu, J. 2004, *Geochimica et Cosmochimica Acta*, 68, 2781
- Frank, M. R., Runge, C. E., Scott, H. P., et al. 2006, *Physics of the Earth and Planetary Interiors*, 155, 152
- French, M., & Redmer, R. 2015, *Phys. Rev. B*, 91, 014308
- Futera, Z., & English, N. J. 2018, *The Journal of Chemical Physics*, 148, 204505
- Goedecker, S., Teter, M., & Hutter, J. 1996, *Phys. Rev. B*, 54, 1703
- Grasset, O., Sotin, C., & Deschamps, F. 2000, *Planetary and Space Science*, 48, 617
- Grindrod, P., Fortes, A., Nimmo, F., et al. 2008, *Icarus*, 197, 137
- Hartwigsen, C., Goedecker, S., & Hutter, J. 1998, *Phys. Rev. B*, 58, 3641
- Heller, R. 2014, *ApJ*, 787, 14
- Heller, R., & Pudritz, R. 2015a, *A&A*, 578, A19
- . 2015b, *ApJ*, 806, 181
- Hester, K. C., Huo, Z., Ballard, A. L., et al. 2007, *J. Phys. Chem. B*
- Hirai, H., Machida, S.-i., Kawamura, T., Yamamoto, Y., & Yagi, T. 2006, *American Mineralogist*, 91, 826
- Hirai, H., Tanaka, T., Kawamura, T., Yamamoto, Y., & Yagi, T. 2003, *Phys. Rev. B*, 68, 172102
- Hirai, H., Uchihara, Y., Fujihisa, K., et al. 2001, *J. Chem. Phys.*, 115, 7066
- ichi Machida, S., Hirai, H., Kawamura, T., Yamamoto, Y., & Yagi, T. 2006, *Physics of the Earth and Planetary Interiors*, 155, 170
- Iess, L., Rappaport, N. J., Jacobson, R. A., et al. 2010, *Science*, 327, 1367
- Iess, L., Jacobson, R. A., Ducci, M., et al. 2012, *Science*, 337, 457
- Jelen, B. I., Giovannelli, D., & Falkowski, P. G. 2016, *Annual Review of Microbiology*, 70, 45, PMID: 27297124
- Journaux, B., Daniel, I., Petitgirard, S., et al. 2017, *Earth and Planetary Science Letters*, 463, 36
- Kadobayashi, H., Hirai, H., Ohfuji, H., Ohtake, M., & Yamamoto, Y. 2018, *The Journal of Chemical Physics*, 148, 164503
- Kalousová, K., Sotin, C., Choblet, G., Tobie, G., & Grasset, O. 2018, *Icarus*, 299, 133
- Kaltenegger, L., Selsis, F., Fridlund, M., et al. 2010, *Astrobiology*, 10, 89, PMID: 20307185
- Kipping, D. M., Fossey, S. J., & Campanella, G. 2009, *Monthly Notices of the Royal Astronomical Society*, 400, 398
- Kirk, R., & Stevenson, D. 1987, *Icarus*, 69, 91
- Krack, M. 2005, *Theoretical Chemistry Accounts*, 114, 145
- Kurnosov, A., Dubrovinsky, L., Kuznetsov, A., & Dmitriev, V. 2006, *zeitschrift fur Naturforschung B*, 61, 1573
- Landau, L. D., & Lifshitz, E. M. 2007, *Statistical physics Part 1*, 3rd edn., Vol. 5 (Butterworth-Heinemann)
- Lee, K., Murray, E. D., Kong, L., Lundqvist, B. I., & Langreth, D. C. 2010, *Phys. Rev. B*, 82, 081101
- Lejaeghere, K., Speybroeck, V. V., Oost, G. V., & Cottenier, S. 2014, *Critical Reviews in Solid State and Materials Sciences*, 39, 1
- Levi, A., Sasselov, D., & Podolak, M. 2013, *The Astrophysical Journal*, 769, 29

- Levi, A., Sasselov, D., & Podolak, M. 2014, *The Astrophysical Journal*, 792, 125
- Lin, J.-F., Militzer, B., Struzhkin, V. V., et al. 2004, *J. Chem. Phys.*, 121, 8423
- Lorenz, R. D., Mitchell, K. L., Kirk, R. L., et al. 2008, *Geophysical Research Letters*, 35, <https://agupubs.onlinelibrary.wiley.com/doi/pdf/10.1029/2007GL032118>
- Loveday, J. S., & Nemes, R. J. 2008, *Phys. Chem. Chem. Phys.*, 10, 937
- Loveday, J. S., Nemes, R. J., Guthrie, M., et al. 2001a, *Let. Nat.*, 410, 661
- Loveday, J. S., Nemes, R. J., Guthrie, M., D., K. D., & Tse, J. S. 2001b, *Phys. Rev. Lett.*, 87, 215501(1)
- Lunine, J., Choukroun, M., Stevenson, D., & Tobie, G. 2010, *The Origin and Evolution of Titan*, ed. Brown, R. H., Lebreton, J.-P., & Waite, J. H., 35–+
- Lunine, J. I. 2009, *Proceedings of the American Philosophical Society*, 153, 403
- Lunine, J. I., & Stevenson, D. J. 1987, *Icarus*, 70, 61
- Macke, R. J., Consolmagno, G. J., & Britt, D. T. 2011, *Meteoritics & Planetary Science*, 46, 1842
- Marques, M., Oliveira, M., & Burnus, T. 2012, *Computer Physics Communications*, 183, 2272
- McKay, C. P. 2014, *Proceedings of the National Academy of Sciences*, 111, 12628
- McKay, C. P. 2016, *Life*, 6, 8
- Mitri, G., Meriggiola, R., Hayes, A., et al. 2014, *Icarus*, 236, 169
- Monteux, J., Tobie, G., Choblet, G., & Feuvre, M. L. 2014, *Icarus*, 237, 377
- Myint, P. C., Benedict, L. X., & Belof, J. L. 2017, *The Journal of Chemical Physics*, 147, 084505
- Niemann, H. B., Atreya, S. K., Demick, J. E., et al. 2010, *Journal of Geophysical Research: Planets*, 115, <https://agupubs.onlinelibrary.wiley.com/doi/pdf/10.1029/2010JE003659>
- Nimmo, F., & Bills, B. 2010, *Icarus*, 208, 896
- Qi, T., & Reed, E. J. 2012, *The Journal of Physical Chemistry A*, 116, 10451, PMID: 23013329
- Reese, C., Solomatov, V., & Baumgardner, J. 2005, *Physics of the Earth and Planetary Interiors*, 149, 361
- Schubert, G., Turcotte, D. L., & Olson, P. 2001, *Mantle Convection in the Earth and Planets*
- Shin, K., Kumar, R., Udachin, K. A., Alavi, S., & Ripmeester, J. A. 2012, *Proceedings of the National Academy of Science*, 109, 14785
- Shin, K., Udachin, K. A., Moudrakovski, I. L., et al. 2013, *Proceedings of the National Academy of Science*, 110, 8437
- Sohl, F., Hussmann, H., Schwentker, B., Spohn, T., & Lorenz, R. D. 2003, *Journal of Geophysical Research: Planets*, 108, n/a, 5130
- Solomatov, V. S. 1995, *Physics of Fluids*, 7, 266
- Tchijov, V. 2004, *Journal of Physics and Chemistry of Solids*, 65, 851
- Thiriet, M., Breuer, D., Michaut, C., & Plesa, A.-C. 2019, *Physics of the Earth and Planetary Interiors*, 286, 138
- Tobie, G., Gautier, D., & Hersant, F. 2012, *The Astrophysical Journal*, 752, 125
- VandeVondele, J., & Hutter, J. 2007, *The Journal of Chemical Physics*, 127, 114105
- VandeVondele, J., Krack, M., Mohamed, F., et al. 2005, *Computer Physics Communications*, 167, 103
- Vosko, S. H., Wilk, L., & Nusair, M. 1980, *Canadian Journal of Physics*, 58, 1200
- Wagner, W., & Pruss, A. 2002, *J. Phys. Chem. Ref. Data*, 31, 387
- Yomogida, K., & Matsui, T. 1983, *Journal of Geophysical Research: Solid Earth*, 88, 9513